Journal of Materials Chemistry A

ROYAL SOCIETY OF CHEMISTRY

PAPER

Published on 10 August 2026

Cite this: DOI: 10.1039/d6ta04885d

Back-contact charge selectivity enables efficient $Cs_2AgBi_2I_9$ indoor photovoltaics under ambient office lighting

Mokurala Krishnaiah, *[a] Akhil Alexander, [a] Adriana Pecoraro, [b] Ramesh Kumar, [c] Joshua K. G. Karlsson,[a] Bidyashakti Dash,[a] Hanmandlu Chintam,[d] K. D. M. Rao, [e] Ana Belén Muñoz-García, [b] Michele Pavone, [f] G. Krishnamurthy Grandhi[a] and Paola Vivo *[a]

Lead-free perovskite-inspired materials are promising absorbers for indoor photovoltaics (IPVs), yet their performance is often limited by interfacial recombination, leakage currents, and non-ideal charge-selective contacts. Here, we demonstrate that the efficiency of $Cs_2AgBi_2I_9$ IPVs is governed by hole-transport-layer (HTL) selectivity rather than by intrinsic hole-injection kinetics alone. Mesoscopic n–i–p devices employing doped Spiro-OMeTAD, P3HT, PCPDTBT, and PPDT2FBT as HTLs were systematically compared under AM 1.5G and white light-emitting diode (WLED) illumination. The PPDT2FBT-based device achieves a power conversion efficiency of 8.50% (8.30% stabilized) under 6500 K, 1000 lux WLED illumination, among the highest reported for wide-bandgap Bi-based IPVs under comparable conditions. By correlating photovoltaic performance with transient photocurrent/photovoltage, electrochemical impedance spectroscopy, dark current–voltage analysis, and interfacial electronic-coupling calculations, we show that faster hole-transfer kinetics alone do not determine device efficiency. Instead, the dominant factor under low-light operation is back-contact selectivity, which governs electron leakage, interfacial recombination, and voltage loss. PPDT2FBT provides the most selective contact, simultaneously enabling efficient charge extraction, suppressed leakage currents, and enhanced recombination resistance, leading to improved open-circuit voltage and fill factor. Finally, proof-of-concept measurements under mixed office illumination, with simultaneous spectral irradiance monitoring at the device plane, confirm stable photovoltaic operation under realistic indoor lighting conditions. These results identify HTL selectivity as a key design parameter for minimizing voltage losses in wide-bandgap perovskite-inspired photovoltaics and establish a general strategy for advancing low-toxicity IPVs toward practical indoor energy harvesting.

Received 9th June 2026
Accepted 10th August 2026

DOI: 10.1039/d6ta04885d

rsc.li/materials-a

1 Introduction

Indoor photovoltaics (IPVs) are emerging as a key enabling technology for powering electronic devices such as wireless sensor networks and distributed Internet of Things (IoT) systems by harvesting readily available ambient light from indoor environments.[1–3] Unlike outdoor photovoltaics, IPVs operate under weak and spectrally structured illumination, typically provided by artificial light sources such as white light-emitting diodes (WLEDs) and fluorescent lamps, as well as diffuse daylight.[1,4,5] Under these low-light conditions, device performance is highly sensitive to non-idealities such as leakage currents, shunt pathways, trap-assisted recombination, and imperfect charge-selective contacts, which can dominate voltage losses and reduce overall efficiency.[1–7] As a result, maximizing IPV performance requires not only suitable absorbers (with appropriate bandgaps, electronic structures, and spectral overlap with indoor light sources) but also careful control of device-level charge selectivity and recombination pathways.

Lead halide perovskites have demonstrated outstanding power conversion efficiencies (PCEs) under indoor illumination, with reported PCEs reaching ≈44% at 1000 lux.[2–4,8] However, concerns related to Pb toxicity remain a significant

[a]Hybrid Solar Cells, Faculty of Engineering and Natural Sciences, Tampere University, P.O. Box 541, Tampere, FI-33014, Finland. E-mail: paola.vivo@tuni.fi; krishrama33@gmail.com

[b]Department of Physics "E. Pancini" University of Naples Federico II, Comp. Univ. Monte Sant'Angelo, Naples 80126, Italy

[c]Light Technology Institute, Karlsruhe Institute of Technology, Karlsruhe, Germany

[d]Department of Chemistry, Angstrom Laboratory, Uppsala University, Box 423, Uppsala, SE 75120, Sweden

[e]School of Applied & Interdisciplinary Sciences, Indian Association for the Cultivation of Science, Jadavpur, Kolkata 700032, India

[f]Department of Chemical Sciences, University of Naples Federico II Comp. Univ. Monte Sant'Angelo, Naples 80126, Italy

barrier for their widespread deployment in indoor applications, particularly in homes, offices, and wearable electronics.[1,2] This has motivated the development of Pb-free perovskite-inspired materials (PIMs), particularly Bi- and Sb-based compounds, as safer alternatives for indoor energy harvesting.[9–12] Among these, $Cs_2AgBi_2I_9$ has emerged as a promising wide-bandgap absorber due to its suitable optoelectronic properties, chemical stability, and straightforward solution processing.[13,14] While recent studies have demonstrated encouraging indoor efficiencies in Bi-based PIMs,[2,13,15] their performance remains limited by substantial voltage losses and incomplete understanding of the governing device physics.[1,2,13] In wide-bandgap PIM-based IPVs, intrinsic material properties such as exciton binding energy, defect formation energy, and electron–phonon coupling set an upper limit to attainable indoor PCE.[1,16] However, approaching this limit critically depends on minimizing device-level losses, particularly those associated with interfacial recombination, leakage currents, and non-ideal charge-selective contacts. In mesoscopic n–i–p architectures, the hole-transporting layer (HTL) forms the back charge-selective contact and therefore plays a central role in determining device performance.[6,10,13,17] Beyond charge selectivity, the HTL can also influence perovskite nucleation, crystallization, morphology, and carrier dynamics when the absorber is deposited directly onto it, particularly in inverted p–i–n architectures.[18,19] An effective HTL must extract photogenerated holes while simultaneously blocking electron leakage toward the metal electrode.[4,5,10,17,20] This selectivity becomes especially important under low-light operation, where the generated photocurrent is small and even weak leakage or recombination pathways can significantly reduce the open-circuit voltage (V_{OC}) and fill factor (FF).[4,5,10,17,20] Previous studies on Bi- and Sb-based IPVs, including (Cu)–Ag–Bi–I and mixed Sb/Bi systems, have shown that HTL selection strongly influences indoor PCE,[10–13] with doped Spiro-OMeTAD (2,2,7,7-tetrakis(*N*,*N*-di-*p*-methoxyphenylamine)-9,9-spirobifluorene) frequently providing competitive performance (*e.g.*, PCE values exceeding 10% under 1000 lux illumination[10] in mixed Sb/Bi PIM systems). Nevertheless, substantial V_{OC} losses remain, motivating the search for alternative HTLs that offer improved charge selectivity and lower recombination losses. Polymeric HTLs have also emerged as promising alternatives due to their tunable energetics and potentially improved interfacial properties. In our recent work, the polymeric HTL poly[(2,5-bis(2-hexyldecyloxy)-phenylene)-*alt*-(5,6-difluoro-4,7-di(thiophen-2-yl) benzo[*c*]-[1,2,5]-thiadiazole)] (PPDT2FBT) enabled enhanced performance in $Cs_2AgBi_2I_9$ devices under both AM 1.5G and indoor illumination across different WLED intensities and colour temperatures,[13] mainly through gains in V_{OC}. However, the physical origin of this improvement remains unclear. In particular, it is not yet established whether device performance is governed primarily by intrinsic hole-transfer kinetics, energetic alignment, interfacial electronic coupling, or by macroscopic factors such as recombination and leakage-current suppression.

Here, we address this question by systematically investigating the role of HTL-dependent back-contact charge selectivity in $Cs_2AgBi_2I_9$ photovoltaics. Mesoscopic n–i–p devices employing doped Spiro-OMeTAD, poly(3-hexylthiophene) (P3HT), poly[2,6-(4,4-bis-(2-ethylhexyl)-4*H*-cyclopenta[2,1-*b*;3,4-*b*′]dithiophene)-*alt*-4,7(2,1,3-benzothiadiazole)] (PCPDTBT), and PPDT2FBT HTLs were compared under AM 1.5G (1-Sun), indoor WLED, and mixed office-light conditions. By combining photovoltaic statistics and external quantum efficiency (EQE) with transient photocurrent (TPC), transient photovoltage (TPV), electrochemical impedance spectroscopy (EIS), dark current–voltage analysis, and interfacial electronic-coupling calculations, we disentangle the contributions of charge-extraction kinetics, recombination, and leakage current. We show that device performance is not governed by hole-injection kinetics alone, but rather by the degree of back-contact selectivity, which controls electron leakage, interfacial recombination, and voltage loss. The optimized PPDT2FBT-based device achieves a PCE of 8.50% under 6500 K, 1000 lux WLED illumination. Finally, motivated by the need to move beyond idealized laboratory conditions, the optimized $Cs_2AgBi_2I_9$/PPDT2FBT device is evaluated under realistic office-light conditions (composed of mixed WLED lighting and diffuse daylight),[4,5] with simultaneous measurement of spectral irradiance at the device plane. These measurements provide a proof-of-concept assessment of device operation under realistic indoor light fields. Overall, this work establishes charge-selective back contacts as a key design principle for reducing voltage losses in wide-bandgap PIM-based IPVs and provides a mechanistic framework for advancing low-toxicity IPVs toward practical indoor energy harvesting.

2 Results and discussion

$Cs_2AgBi_2I_9$ absorber films were prepared using the solution-processing procedure described in the Experimental section. Structural, compositional, morphological, optical, and photophysical characterization is summarized in Fig. S1–S6, SI. The XRD pattern and Raman mapping support the formation and lateral uniformity of crystalline $Cs_2AgBi_2I_9$, while XPS and EDS confirm the incorporation of Cs, Ag, Bi, and I with near-stoichiometric composition. AFM and SEM images show compact film coverage, and optical absorption measurements give a bandgap of approximately 1.8 eV, consistent with the spectral requirements for WLED-based IPVs. Transient-absorption measurements on bare $Cs_2AgBi_2I_9$ films reveal photoinduced features in the 450–520 nm region, with sub-picosecond carrier cooling followed by longer-lived relaxation components, consistent with previous reports.[13,14] Because these measurements probe the intrinsic absorber dynamics without an HTL, the following discussion focuses on HTL-dependent back-contact charge selectivity, recombination, leakage current, and voltage retention in complete devices.

The verified $Cs_2AgBi_2I_9$ films were then incorporated into mesoscopic n–i–p photovoltaic devices with the architecture glass/patterned FTO/compact TiO_2/mesoporous TiO_2/$Cs_2AgBi_2I_9$/HTL/Au, as illustrated in Fig. 1a. The cross-sectional SEM image of a representative device, presented in Fig. S7 of the SI, verifies the formation of the multilayer device stack, where the FTO, compact TiO_2, mesoporous TiO_2/$Cs_2AgBi_2I_9$, PPDT2FBT,

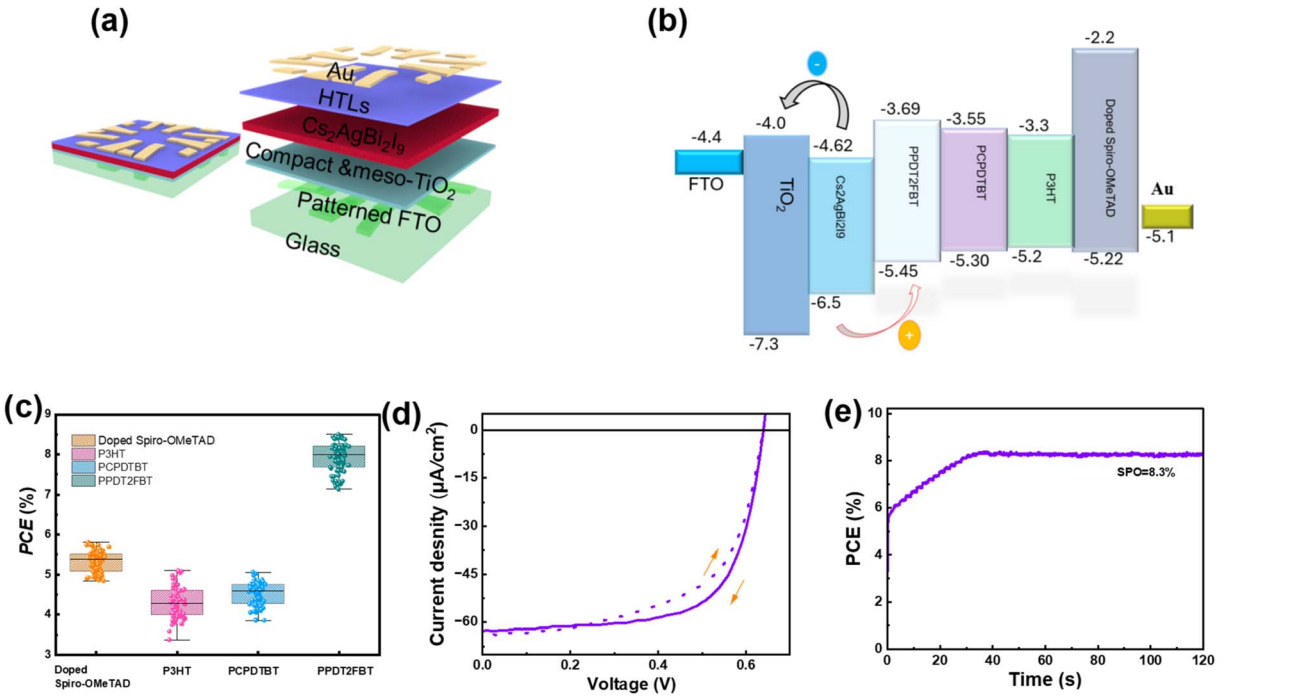

Fig. 1 HTL-dependent device architecture, energy alignment, and indoor photovoltaic performance of $Cs_2AgBi_2I_9$ devices: (a) schematic illustration of the mesoscopic n–i–p device architecture: glass/patterned FTO/compact TiO_2/mesoporous TiO_2/$Cs_2AgBi_2I_9$/HTL/Au. (b) Energy-level diagram of $Cs_2AgBi_2I_9$ devices employing different hole-transporting layers, including PPDT2FBT, PCPDTBT, P3HT, and doped Spiro-OMeTAD. (c) Statistical distribution of power conversion efficiency (η) of $Cs_2AgBi_2I_9$ devices with different HTLs under indoor WLED illumination. (d) Current density–voltage (J–V) curves (arrows indicate the reverse and forward scan directions) of the champion PPDT2FBT-based $Cs_2AgBi_2I_9$ indoor photovoltaic device measured under WLED illumination at 6500 K and 1000 lux, corresponding to an incident power density of 330 μW cm^{-2}. (e) Stabilized power output measured at the maximum power point, giving an SPO of 8.3%.

and Au electrode layers can be distinguished. To isolate the role of the back hole contact, all devices were fabricated using the same absorber-processing route and mesoscopic n–i–p architecture, while only the HTL was varied. Doped Spiro-OMeTAD, P3HT, PCPDTBT, and PPDT2FBT were selected to compare a conventional molecular HTL with conjugated polymeric HTLs having different energetic alignment, molecular geometry, and interfacial electronic coupling with $Cs_2AgBi_2I_9$. This design allows the HTL-dependent changes in photovoltaic output to be linked primarily to the $Cs_2AgBi_2I_9$/HTL back interface. Because $Cs_2AgBi_2I_9$ was deposited and annealed before HTL coating, the HTLs were not involved in its initial nucleation or bulk crystallization. The observed differences are therefore attributed primarily to the subsequently formed $Cs_2AgBi_2I_9$/HTL interface, although local surface modifications during HTL deposition cannot be excluded.

The literature-derived energy-level diagram in Fig. 1b places the CBM and VBM of $Cs_2AgBi_2I_9$ at approximately −4.62 and −6.50 eV, respectively. PPDT2FBT has reported LUMO and HOMO levels of approximately −3.69 and −5.45 eV, with a frontier-orbital separation of approximately 1.76 eV.[13,21,22] Among the investigated HTLs, PPDT2FBT therefore provides the smallest nominal HOMO-VBM offset of approximately 1.05 eV while retaining an electron-blocking offset of approximately 0.93 eV. Nevertheless, energy-level alignment alone does not determine HTL suitability; the superior performance of PPDT2FBT reflects the combined effects of energetic alignment, interfacial coupling, charge extraction, recombination suppression, and leakage-current control. Therefore, the photovoltaic response was first compared statistically under both AM 1.5G and indoor WLED illumination before analysing the underlying charge-extraction and recombination processes.

The photovoltaic performance of $Cs_2AgBi_2I_9$ devices employing different HTLs was initially assessed under simulated AM 1.5G, 100 mW cm^{-2} illumination. As summarized in Fig. S8 and S9 of the SI, the choice of HTL has a pronounced effect on the photovoltaic performance, including J_{SC}, V_{OC}, FF, and PCE. Among the investigated HTLs, PPDT2FBT yields the best average device performance, with a PCE of 3.44 ± 0.22%, J_{SC} of 6.27 ± 0.45 mA cm^{-2}, V_{OC} of 0.77 ± 0.016 V, and FF of 68.01 ± 1.88%. By comparison, devices based on PCPDTBT, P3HT, and doped Spiro-OMeTAD exhibit lower average PCEs of 2.37 ± 0.15%, 1.90 ± 0.125%, and 1.51 ± 0.219%, respectively. The same trend is observed for the champion devices, where the PPDT2FBT-based device reaches a PCE of 3.70%, exceeding those of PCPDTBT, P3HT, and doped Spiro-OMeTAD devices, which deliver champion PCEs of 2.69%, 2.21%, and 2.26%, respectively. The champion current density–voltage (J–V) characteristics shown in Fig. S10a are consistent with the statistical results in Fig. S9 (Table S1 in SI), further demonstrating the HTL-dependent nature of the $Cs_2AgBi_2I_9$ photovoltaic performance. The improved performance of the PPDT2FBT-based

devices is reflected in simultaneous enhancement of J_{SC}, V_{OC}, and FF, suggesting more efficient charge collection and reduced interfacial recombination at the $Cs_2AgBi_2I_9$/PPDT2FBT interface. The EQE spectra in Fig. S10b show that the PPDT2FBT-based device provides the strongest photoresponse in the visible region. Stabilized power output (SPO) measurements were then performed to evaluate steady-state device operation under continuous illumination. As shown in Fig. S11 of the SI, all devices exhibit a rapid increase in output, followed by stabilized SPO plateaus. The PPDT2FBT-based device maintains the highest stabilized output among the investigated HTLs, indicating that its excellent performance is not an artifact of transient *J–V* scan behaviour but reflects improved steady-state operation.

To place the 1-Sun performance of the present devices in context, the champion photovoltaic parameters were compared with those reported for representative Bi-based perovskite-inspired photovoltaic devices in the literature, as summarized in Table S2 of the SI. The PPDT2FBT-based $Cs_2AgBi_2I_9$ device delivers a champion PCE of 3.70%, with a $J_{SC} = 7$ mA cm^{-2}, $V_{OC} = 0.792$ V, and FF = 67%. This PCE value is comparable to or higher than many existing Bi-PIMs, including $AgBiI_4$, Ag_2BiI_5, Ag_3BiI_6, Cu_2AgBiI_6 (Table S2, SI). The EQE-integrated J_{SC} of ~8 mA cm^{-2} is consistent with the J_{SC} used to calculate the champion 1-Sun PCE, supporting reasonable agreement between EQE and *J–V* measurements.

A clear HTL-dependent behaviour is observed under indoor WLED illumination at 6500 K and 1000 lux (Fig. 1c), corresponding to an incident power density of 330 μW cm^{-2}. As shown in Fig. S8, the PPDT2FBT-based device achieves the highest indoor PCE of 8.50%, outperforming the doped Spiro-OMeTAD, P3HT, and PCPDTBT-based devices, which deliver PCEs of 5.90%, 5.10%, and 5.06%, respectively. Although the performance ranking between the HTLs differs slightly between AM 1.5G and indoor WLED operation, PPDT2FBT consistently enables the highest efficiency under both illumination conditions. The statistical distributions of the IPV parameters obtained from 50 devices, shown in Fig. 1c and Fig. S12, support the reproducibility of this trend. The champion indoor *J–V* curves measured under 1000 lux illumination (Fig. 1d) further demonstrate the superior low-light response of the PPDT2FBT-based device, while the steady-state PCE reaches 8.30% (Fig. 1e), supporting stable indoor operation under continuous WLED illumination. The indoor PCE of 8.50% is slightly higher than the 7.60% reported in our previous $Cs_2AgBi_2I_9$ IPV study under comparable WLED conditions.[13] This small performance enhancement should be primarily attributed to matured device-fabrication reproducibility, which guarantees a highly reliable baseline for this work. The present study investigates why PPDT2FBT provides the most effective back contact by correlating device performance with charge extraction, recombination suppression, leakage reduction, and voltage retention, thereby establishing interfacial charge selectivity as a key design principle for wide-bandgap perovskite-inspired IPVs.

The EQE-integrated J_{SC} under the WLED photon-flux spectrum is 62.46 μA cm^{-2}, which agrees well with the *J–V* derived J_{SC} of 63.80 μA cm^{-2}, with a deviation of less than 3% (Fig. S13). This close agreement is particularly important for IPV measurements, where current overestimation can occur if the incident spectrum or power density is not accurately determined. The 8.30% stabilized indoor PCE corresponds to a maximum output power density of approximately 27.4 μW cm^{-2} under 330 μW cm^{-2} incident power density, or 2.74 μW total output power for the 10 mm^2 masked device area. The device had overall dimensions of 10 × 10 mm^2. After 10 days of storage, the PPDT2FBT-based device showed closely overlapping *J–V* curves under identical 6500 K, 1000 lux WLED measurement conditions, indicating good short-term stability under the tested conditions (Fig. S14, SI). The champion device also retains relatively stable performance across different WLED colour temperatures, with PCEs of 8.50%, 7.80%, and 7.45% under 6500, 5000, and 4000 K illumination, respectively. The higher PCE values obtained under 1000 lux indoor illumination compared with 1-Sun operation can be associated with the favourable optical response and recombination behaviour of $Cs_2AgBi_2I_9$ under low-light conditions. Its optical bandgap of approximately 1.8 eV enables efficient harvesting of the indoor light emission.[13] Moreover, the lower photogenerated carrier density under indoor illumination can reduce bimolecular or carrier-density-dependent recombination losses and help maintain a high fill factor, enabling higher efficiency under weak indoor light despite the lower absolute current density.[2,13,23] In contrast, under 1-Sun (AM 1.5G) illumination, the higher photon flux can promote carrier accumulation and interfacial recombination, particularly at the $Cs_2AgBi_2I_9$/HTL and TiO_2/$Cs_2AgBi_2I_9$ interfaces. Overall, these results show that HTL strongly influences $Cs_2AgBi_2I_9$ device performance under both AM 1.5G and indoor WLED operating conditions, motivating a deeper analysis of charge extraction, recombination, and leakage current at the $Cs_2AgBi_2I_9$/HTL interface.

To understand the origin of the HTL-dependent photovoltaic behaviour, charge-extraction kinetics and interfacial electronic coupling were examined (Fig. 2). The statistical distribution of J_{SC} values for $Cs_2AgBi_2I_9$ devices employing doped Spiro-OMeTAD, P3HT, PCPDTBT, and PPDT2FBT as HTLs under indoor WLED illumination is presented in Fig. 2a. The J_{SC} follows the order PPDT2FBT > PCPDTBT > P3HT > doped Spiro-OMeTAD, showing that PPDT2FBT enables the most effective photocurrent generation among the investigated back contacts. This trend is consistent with the higher output of PPDT2FBT-based devices and suggests improved charge collection and/or reduced recombination losses at the $Cs_2AgBi_2I_9$/HTL interface. TPC measurements were then carried out to probe the charge-extraction dynamics in the devices with the four HTLs. Unlike the bare-film transient-absorption measurements, these complete-device TPC measurements directly probe HTL-dependent charge-extraction dynamics. As shown in Fig. 2b, devices employing polymeric HTLs exhibit faster normalized photocurrent decay than the doped Spiro-OMeTAD-based device, indicating more efficient charge extraction and a shorter carrier residence time. Among the investigated HTLs, the PPDT2FBT-based device shows the most rapid TPC decay, supporting rapid device-level extraction of photogenerated holes across the $Cs_2AgBi_2I_9$/HTL interface. By contrast, the

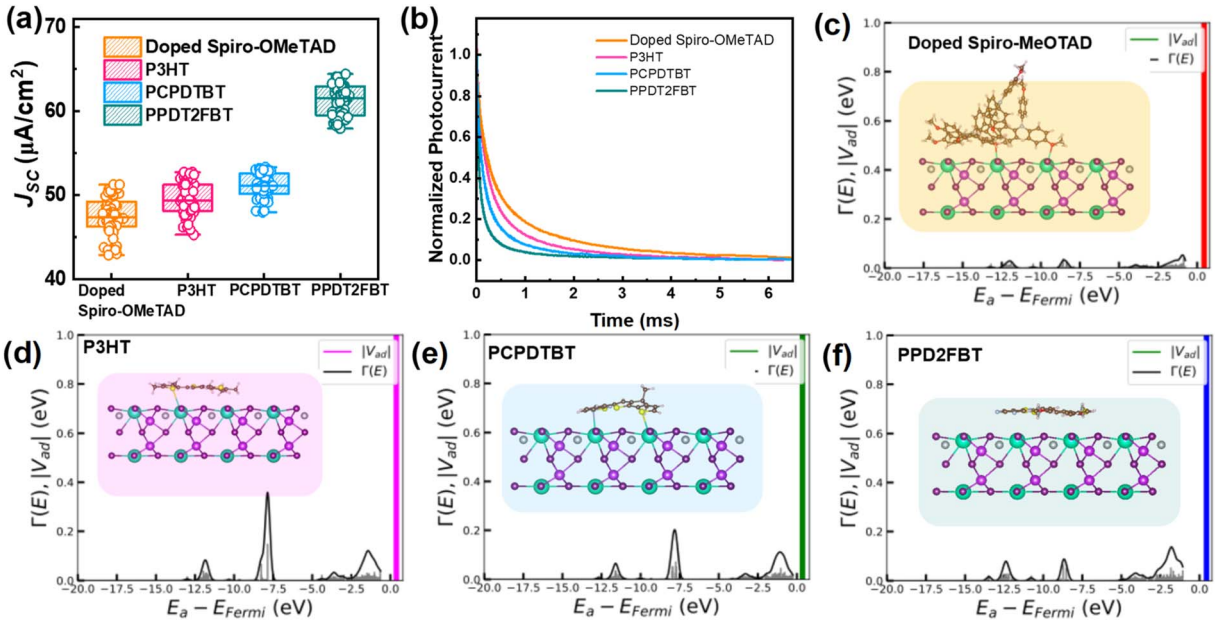

Fig. 2 Charge extraction and interfacial electronic-coupling analysis of $Cs_2AgBi_2I_9$ devices with different HTLs: (a) statistical distributions of the short-circuit current density, J_{SC}, of $Cs_2AgBi_2I_9$ IPV devices (measured under 6500 K, 1000 lux WLED illumination) employing doped Spiro-OMeTAD, P3HT, PCPDTBT, and PPDT2FBT as hole-transporting layers. (b) Normalized transient photocurrent (TPC) decay profiles of $Cs_2AgBi_2I_9$ devices with different HTLs. Calculated interfacial electronic coupling strength, $|V_{ad}|$, and spectral distribution, $\Gamma(E)$, for $Cs_2AgBi_2I_9$ interfaced with (c) doped Spiro-OMeTAD, (d) P3HT, (e) PCPDTBT, and (f) PPDT2FBT.

slower decay observed for doped Spiro-OMeTAD indicates a slower charge extraction, which may increase carrier accumulation and recombination at the absorber/back-contact interface.

To complement the experimental charge-extraction analysis, idealized $Cs_2AgBi_2I_9$/HTL interface models were evaluated using projected density of states and projection-operator diabatization (POD) calculations (Fig. 2c–f)). Details of the slab construction, adhesion and binding-energy definitions, pDOS analysis, and POD formalism, which have been successfully employed in other works,[24–26] are provided in SI Note 2 and Fig. S15–S17 of the SI. The calculations show that all investigated HTLs possess frontier states suitably positioned for hole transfer from $Cs_2AgBi_2I_9$ to the HTL. However, the calculated interfacial properties also show that neither adhesion strength nor intrinsic hole-injection time alone explains the device-performance trend. Spiro-OMeTAD shows the strongest calculated adhesion energy of −3.90 eV but the slowest calculated hole-injection time of 12.22 fs, indicating that strong interfacial adhesion does not necessarily lead to efficient hole transfer. In contrast, the polymeric HTLs show substantially faster calculated injection times of between 1.83–4.79 fs (1.83 fs for P3HT, 3.26 fs for PCPDTBT, and 4.79 fs for PPDT2FBT, Table S3 in SI). The faster calculated injection times for the polymeric HTLs are broadly consistent with their faster TPC decay compared with doped Spiro-OMeTAD (Fig. 2b). However, because P3HT exhibits the shortest calculated injection time without delivering the best device performance, injection kinetics alone cannot explain the observed device trend. Instead, efficient $Cs_2AgBi_2I_9$ device operation requires a balanced interfacial electronic coupling, favourable energetic alignment, effective charge selectivity, and suppression of recombination and leakage losses. Among the investigated HTLs, PPDT2FBT provides the best overall balance of these factors: it exhibits rapid device-level TPC response, suitable molecular-level coupling, and the highest J_{SC} and PCE in complete devices. Therefore, the superior performance of PPDT2FBT-based $Cs_2AgBi_2I_9$ devices cannot be assigned simply to faster hole injection. Rather, it arises from sufficiently efficient charge extraction combined with reduced recombination and improved back-contact selectivity. This conclusion motivates the following analysis of HTL-dependent voltage loss, recombination resistance, leakage current, and electron-blocking behaviour.

Building on the charge-extraction analysis in Fig. 2, we next examined how the HTL governs voltage retention, recombination, leakage current, and back-contact charge selectivity in $Cs_2AgBi_2I_9$ photovoltaic devices. While efficient hole extraction is essential for enhancing photocurrent generation, the final V_{OC} and FF are also strongly affected by recombination at the $Cs_2AgBi_2I_9$/HTL interface, parasitic leakage pathways, shunt behaviour, and the ability of the HTL to block electron leakage toward the Au electrode.[27–30] Therefore, V_{OC} statistics, electrochemical impedance spectroscopy (EIS), dark current analysis, differential resistance measurements, and transient photovoltage (TPV) measurements were used together to elucidate the origin of HTL-dependent voltage losses. As shown in Fig. 3a, the V_{OC} distribution is strongly HTL-dependent. The PPDT2FBT-based device delivers the highest V_{OC} among the investigated devices, indicating lower voltage loss at the $Cs_2AgBi_2I_9$/HTL

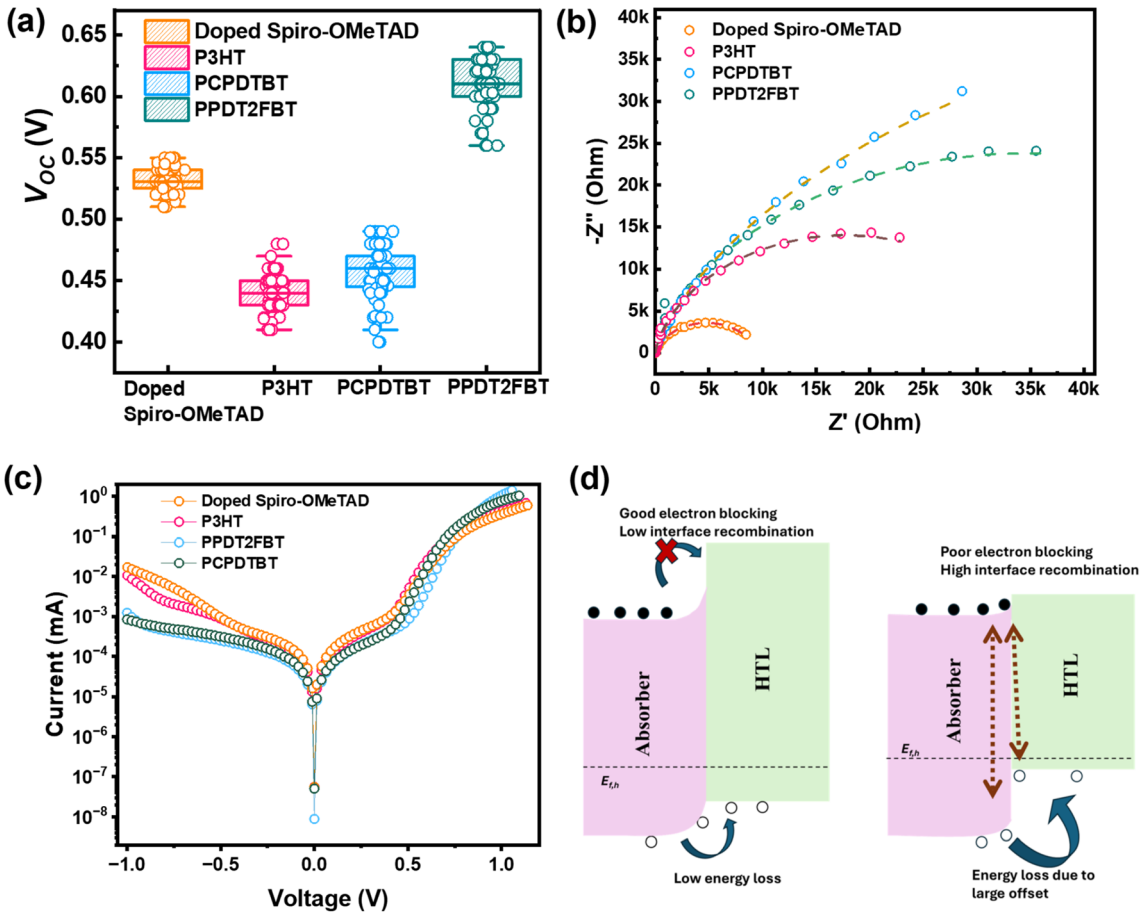

Fig. 3 HTL-dependent voltage retention, recombination resistance, leakage suppression, and proposed back-contact mechanism in $Cs_2AgBi_2I_9$ indoor photovoltaic devices: (a) statistical distribution of open-circuit voltage, V_{OC}, for $Cs_2AgBi_2I_9$ devices employing different HTLs. (b) Nyquist plots obtained from electrochemical impedance spectroscopy, showing HTL-dependent recombination and charge-transfer resistance. (c) Dark current–voltage characteristics of $Cs_2AgBi_2I_9$ devices with different HTLs, highlighting leakage-current suppression and rectification behaviour. (d) Schematic illustration of the proposed HTL-dependent interfacial mechanism: a selective HTL supports hole extraction while suppressing electron leakage and interfacial recombination, whereas a less selective HTL allows electron leakage, enhanced interfacial recombination, and increased voltage loss.

interface. This behaviour indicates that PPDT2FBT forms a more selective back contact that promotes hole collection while suppressing electron leakage and recombination near the Au electrode. By contrast, the lower V_{OC} values obtained for doped Spiro-OMeTAD, P3HT, and PCPDTBT indicate larger back-interfacial losses and less effective charge selectivity. The EIS Nyquist plots in Fig. 3b provide comparative insight into HTL-dependent recombination behaviour. The extracted parameters are summarized in Table S4 of the SI. The PPDT2FBT-based device exhibits the largest recombination resistance, R_{rec}, of 36.24 kΩ, followed by PCPDTBT, P3HT, and doped Spiro-OMeTAD with values of 28.20, 22.80, and 8.37 kΩ, respectively. Since a higher R_{rec} corresponds to slower recombination, the recombination tendency follows the order doped Spiro-OMeTAD > P3HT > PCPDTBT > PPDT2FBT. Thus, the EIS results support reduced recombination losses in the PPDT2FBT-based device, consistent with its higher V_{OC} and improved device performance. The EIS-derived series resistance, R_s, also depends on the HTL. PCPDTBT shows the lowest R_s of 9.2 Ω, followed by P3HT, PPDT2FBT, and doped Spiro-OMeTAD with values of 12.5, 17.5, and 23.9 Ω, respectively. Although PCPDTBT exhibits the lowest series resistance (R_s), its overall device efficiency remains lower than that of PPDT2FBT. This indicates that reducing R_s alone is not sufficient to maximize the device performance. Instead, suppression of recombination and leakage losses is more important for maximizing $Cs_2AgBi_2I_9$ device output, particularly under low-light indoor conditions.[1,31,32]

The dark current–voltage curves in Fig. 3c provide additional insight into leakage behavior and diode quality. The PPDT2FBT-based device shows the lowest ideality factor of 1.74, the lowest saturation current of 6.74×10^{-12} A, the highest shunt resistance of 1.69 MΩ, and the lowest series resistance of 160 Ω compared with the other HTL-based devices. These parameters are consistent with reduced trap-assisted recombination, suppressed leakage pathways, and improved charge-selective transport (Table S5 in SI). In comparison, the doped Spiro-OMeTAD-based device exhibits a higher ideality factor of 2.55,

a larger saturation current of 1.54×10^{-9} A, a lower shunt resistance of 0.69 MΩ, and a higher series resistance of 561 Ω, consistent with stronger recombination and less effective leakage suppression. The approximately two-order-of-magnitude reduction in saturation current in the case of PPDT2FBT HTL compared with doped Spiro-OMeTAD is particularly important for IPVs, where the photocurrent is low and dark leakage can strongly limit V_{OC} and FF.[13,33,34] The differential resistance curves in Fig. S18 of the SI supports the same conclusion. A higher differential resistance in the reverse-bias and low-bias regions reflects more effective suppression of leakage current and shunt pathways, which is beneficial for maintaining high V_{OC} under low-light operation.

The PPDT2FBT-based device shows improved resistance behaviour compared with the other HTLs, suggesting reduced parasitic current flow and improved voltage retention at the back contact. TPV measurements, shown in Fig. S19 and summarized in Table S4 of the SI, further support the HTL-dependent recombination behavior. The PPDT2FBT-based device exhibits the longest recombination lifetime of 10.9 μs, closely followed by PCPDTBT with 10.5 μs. Doped Spiro-OMeTAD and P3HT show shorter lifetimes of 8.14 μs and 4.04 μs, respectively.

Although the PPDT2FBT- and PCPDTBT-based devices show comparable TPV lifetimes of 10.9 and 10.5 μs, respectively, this similarity does not necessarily imply identical steady-state recombination losses or identical V_{OC} values. TPV probes the relaxation of a small photovoltage perturbation around the open-circuit operating point and may be influenced by carrier density, differential resistance, and device capacitance.[35–38] Therefore, lifetime should be interpreted together with complementary electrical measurements. Compared with the PPDT2FBT-based device, the PCPDTBT-based device exhibits a lower recombination resistance, an approximately 11.6-fold higher dark saturation current, a higher ideality factor, and a slightly lower shunt resistance (Tables S4 and S5). The higher dark saturation current is particularly relevant because V_{OC} depends logarithmically on the balance between photogenerated current and recombination or dark current. These differences indicate larger steady-state recombination and leakage losses in the PCPDTBT-based device, explaining its lower V_{OC} despite the similar TPV decay time. Overall, the TPC and TPV results demonstrate that HTL selection influences both charge-extraction and recombination dynamics.

Based on these combined electrical measurements, we propose an interfacial recombination mechanism, as illustrated in Fig. 3d. An effective HTL should enable selective hole extraction while suppressing electron transfer toward the Au electrode. It should also reduce interfacial recombination and minimize voltage loss at the $Cs_2AgBi_2I_9$/HTL contact. Among the investigated HTLs, PPDT2FBT best satisfies these requirements. Its favourable interfacial energetics and electron-blocking ability, *i.e.*, back-contact selectivity, promote selective hole transport while reducing electron leakage and recombination at the rear electrode. This suppresses charge accumulation, lowers recombination at the back interface, and reduces voltage loss.[13,39,40] In contrast, less selective HTLs can introduce larger energetic offsets or weaker electron-blocking behaviour, resulting in enhanced electron leakage, stronger recombination, and diminished V_{OC} and FF. Under indoor illumination at 1000 lux, all devices exhibit higher PCEs than under 1-Sun illumination, which can be partly attributed to reduced carrier-density-dependent recombination at lower photogenerated carrier densities. The indoor PCE follows the order PPDT2FBT > doped Spiro-OMeTAD > P3HT > PCPDTBT. Although doped Spiro-OMeTAD exhibited relatively low recombination resistance in the EIS analysis, its improved response under indoor illumination suggests that recombination losses become less pronounced at reduced carrier densities. In comparison, PPDT2FBT delivered the highest efficiency under both 1-Sun and indoor conditions, confirming its effectiveness across different illumination regimes. This improvement is attributed to efficient device-level charge extraction, reduced electron leakage, suppressed interfacial recombination, and improved voltage retention. The combination of the highest recombination resistance, longest TPV lifetime, lowest saturation current, and highest shunt resistance further indicates that PPDT2FBT provides the most effective charge-selective back contact among the investigated HTLs. These results indicate that optimizing HTLs for $Cs_2AgBi_2I_9$ photovoltaics requires simultaneous control of charge extraction, electron leakage, interfacial recombination, and voltage loss.

Based on these findings, a representative $Cs_2AgBi_2I_9$/PPDT2FBT device was further evaluated under mixed office-light illumination, as shown in Fig. 4, as a proof-of-concept assessment of low-light operation under practical indoor lighting conditions. Recent IPV metrology studies have emphasized the need to evaluate devices under device-plane mixed illumination conditions, rather than relying solely on idealized single-source lighting.[4,5,7] The office-light test was performed under ambient indoor illumination, as shown in Fig. 4a. Unlike calibrated WLED measurements, the office environment provides a mixed, spatially non-uniform, and time-dependent light field composed of artificial room lighting, local workspace illumination, and diffuse daylight contributions. This setting approximates practical operating conditions for low-power electronics and IoT nodes. The spectral irradiance profiles recorded simultaneously with the photovoltaic measurements at different times of the day are shown in Fig. 4b and compared with a reference WLED spectrum measured at 1000 lux. Because the measured office-light correlated colour temperature varied between approximately 4100 and 4500 K during the measurement period, a 4000 K, 1000 lux WLED spectrum was used as the closest controlled reference for this proof-of-concept mixed-light comparison. The 6500 K, 1000 lux WLED measurements discussed above remain the controlled benchmark condition used for the champion indoor device performance. The office-light spectra exhibit visible emission with a blue component around 430–470 nm and a broad visible band, while both spectral composition and incident power density vary with time due to changing daylight contributions. To reduce photocurrent overestimation, the office-light *J–V* measurements were performed using the same 10 mm^2 aperture mask as used for the controlled indoor measurements. The

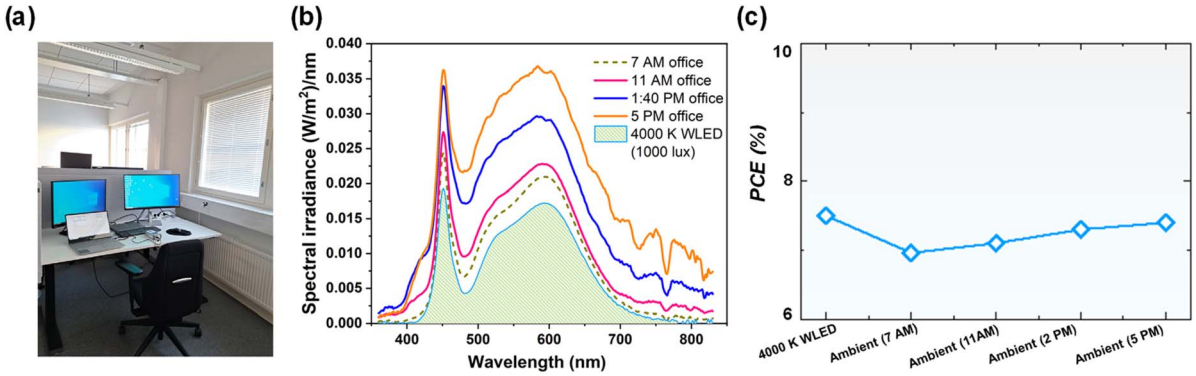

Fig. 4 Proof-of-concept mixed office-light operation of a representative $Cs_2AgBi_2I_9$/PPDT2FBT device. (a) Photograph of the office environment used for mixed indoor-light testing. (b) Spectral irradiance profiles of ambient office illumination recorded simultaneously with the photovoltaic measurements at different times of the day during office working hours. A 4000 K, 1000 lux WLED spectrum is included as a controlled reference because the measured office-light correlated colour temperature varied between approximately 4110 and 4524 K during the measurement period. (c) PCE of a representative $Cs_2AgBi_2I_9$/PPDT2FBT device under the 4000 K, 1000 lux WLED reference condition and mixed office-light conditions.

PCE values were calculated using the simultaneously measured spectral irradiance at the device plane. Under these non-standard and fluctuating illumination conditions, the $Cs_2AgBi_2I_9$/PPDT2FBT device retains measurable low-light photovoltaic output. As shown in Fig. 4c, the device delivers a PCE of approximately 7.5% under the controlled indoor WLED reference condition and retains a PCE close to 7% under mixed office-light illumination measured at different times of the day. The variation in PCE is attributed to changes in incident power density, spectral composition, and spatial illumination uniformity. These measurements should therefore be regarded as a proof-of-concept evaluation of mixed-light operation in Bi-based PIM IPVs rather than a full quantitative assessment of deployment-relevant performance.

3 Conclusion

In summary, we have demonstrated that the performance of $Cs_2AgBi_2I_9$-based photovoltaic devices is strongly governed by HTL-dependent back-contact charge selectivity under both AM 1.5G and indoor WLED illumination. Mesoscopic n–i–p devices employing doped Spiro-OMeTAD, P3HT, PCPDTBT, and PPDT2FBT as HTLs showed clear differences in photocurrent generation, voltage retention, recombination, and leakage behavior. Among these HTLs, PPDT2FBT delivered the best performance, reaching a PCE of 3.70% under AM 1.5G illumination and 8.50% under 6500 K, 1000 lux WLED illumination. The combined TPC, TPV, EIS, dark current–voltage, and interfacial electronic-coupling analyses indicate that the superior performance of the PPDT2FBT-based device is not determined by intrinsic hole-injection kinetics alone. In fact, PPDT2FBT provides the best overall balance of charge extraction, recombination suppression, leakage-current reduction, and voltage retention at the $Cs_2AgBi_2I_9$/HTL back interface.

As an initial step toward practical indoor evaluation, a representative $Cs_2AgBi_2I_9$/PPDT2FBT device was assessed under mixed office-light illumination. Under these proof-of-concept conditions, the device retained stable photovoltaic output under ambient indoor illumination composed of WLED light and diffuse daylight. Future studies should include angle-dependent response and position-dependent irradiance mapping under mixed indoor light. Overall, this work establishes back-contact charge selectivity as a key interfacial design principle for advancing low-toxicity, wide-bandgap perovskite-inspired photovoltaics toward practical indoor energy harvesting.

4 Experimental details

4.1 Materials and preparation of $Cs_2AgBi_2I_9$ films

Bismuth iodide (BiI_3, 99.99%), cesium iodide (CsI, 99.99%), silver iodide (AgI, 99.99%), hydroiodic acid (HI, 57%), chlorobenzene (CB, extra dry, 99.8%), acetonitrile (99.9%), 4-*tert*-butylpyridine (4-*t*BP), lithium bis(trifluoromethanesulfonyl) imide (Li-TFSI, 99.95%), titanium diisopropoxide bis(acetylacetonate) solution (75 wt% in 2-propanol), and anhydrous 2-propanol (99.5%) were obtained from Sigma-Aldrich. Tris[2-(1*H*-pyrazol-1-yl)-4-*tert*-butylpyridine]cobalt(III) tris[bis(trifluoromethanesulfonyl)imide] (FK209 Co(III), >98%) was supplied by Dyenamo. Anhydrous *N*,*N*-dimethylformamide (DMF, 99.8%) and anhydrous dimethyl sulfoxide (DMSO, 99.8%) were obtained from Alfa Aesar. Spiro-OMeTAD was sourced from Lumtec, PCPDTBT from Brilliant Matters, poly(3-hexylthiophene-2,5-diyl) (P3HT, electronic grade, regioregular) was purchased from Rieke Metals, PPDT2FBT from 1-Material, and 30 NR-D TiO_2 nanoparticle paste from Greatcell Solar Materials. All reagents were used directly without additional purification.

$Cs_2AgBi_2I_9$ thin films were prepared using a procedure adapted from our previous work.[13] The precursor solution was prepared by dissolving CsI, AgI, and BiI_3 in 1 mL of DMF : DMSO mixed solvent, 4 : 1 by volume, using a molar ratio of 2 : 1 : 2. HI, 2 vol%, was added to aid complete dissolution of the precursors and compensate for possible iodine loss during

thermal processing. The solution was stirred magnetically at 600 rpm overnight, approximately 12 h, at room temperature inside a nitrogen-filled glovebox.

For film deposition, 60 μL of the $Cs_2AgBi_2I_9$ precursor solution was cast onto glass or mesoporous TiO_2-coated substrates and spin-coated at 4000 rpm for 20 s. After 6 s of spinning, 150 μL of chlorobenzene was introduced as an antisolvent to assist uniform film formation. The as-deposited precursor films were then treated using a two-step annealing process: first at 130 °C for 5 min, followed by a second annealing step at 225 °C for 3 min. After annealing, the films were used for structural, morphological, compositional, optical, photophysical, and photovoltaic analyses.

4.2 Thin-film characterization

4.2.1 X-ray photoelectron spectroscopy (XPS). X-ray photoelectron spectroscopy (XPS) was used to analyze the surface composition and chemical states of the $Cs_2AgBi_2I_9$ films. The films were prepared on indium tin oxide (ITO)-coated glass substrates and kept overnight in a vacuum desiccator to remove residual volatile species before being transferred into the ultrahigh-vacuum (UHV) analysis chamber. Spectra were recorded using non-monochromatized Al $K\alpha_{1,2}$ radiation with a photon energy of 1486.6 eV from a twin-anode X-ray source (8025 Twin Anode, V. G. Microtech). The emitted photoelectrons were detected using a hemispherical electron energy analyser (CLAM4 MCD LNo5, V. G. Microtech). The acquired spectra were processed and fitted using CasaXPS software, version 2.3.25 PR1.0. Before peak fitting, a Shirley background was subtracted, and the core-level components were fitted using Gaussian–Lorentzian line shapes. The binding energy scale was calibrated using the C 1s C–C peak at 284.8 eV.

4.2.2 Atomic force microscopy studies (AFM). Atomic force microscopy studies (AFM) were performed using a Bruker Dimension Icon microscope under ambient conditions at room temperature. High-resolution surface topography was first obtained in Peak Force tapping mode using a Bruker SCANASYST-AIR probe. The samples were scanned over areas ranging from 0.5 to 5 μm^2 with scan rates between 0.5 and 1 Hz. The force setpoint was automatically optimized by the instrument and typically remained within 1–4 nN. The lift height was generally maintained between 140 and 150 nm. After probe-sample contact, the feedback gain and setpoint were automatically adjusted by the instrument. No external electrical bias or additional illumination were applied during the measurements. The films were deposited on conductive glass substrates (fluorine-doped tin oxide coated glass slides). Analysis of AFM images were conducted with the freely available Gwyddion software suite (version 2.64).[41]

4.2.3 Raman mapping and spectroscopic analysis. Raman mapping was carried out to examine the lateral uniformity and phase distribution of the $Cs_2AgBi_2I_9$ thin film. Measurements were performed using a Renishaw inVia Qontor confocal Raman microscope equipped with a 785 nm excitation laser, a high-resolution grating monochromator, and a charge-coupled device detector. During data acquisition, the laser power was limited to 5% to reduce local heating and avoid possible laser-induced changes in the film. The laser was focused on the film surface through a 50× objective lens. Spectra were acquired sequentially from individual points within the selected rectangular mapping area, which corresponds to the optical micrograph shown with a 20 μm scale bar. The Raman intensity of a representative vibrational band was then used to generate the false-color intensity map.

4.2.4 Scanning electron microscopy (SEM). The surface morphology of $Cs_2AgBi_2I_9$ films deposited on FTO/compact TiO_2/mesoporous TiO_2 substrates was examined by top-view scanning electron microscopy (SEM). Before imaging, the samples were coated with a 5 nm carbon layer to reduce charging effects. SEM images were acquired using a Zeiss Ultra Plus field-emission scanning electron microscope operated in secondary electron mode. Additional SEM images of $Cs_2AgBi_2I_9$ films deposited on FTO and compact TiO_2 substrates were also collected using the same Zeiss Ultra Plus field-emission scanning electron microscope. The measurements were performed at an acceleration voltage of 5 kV. Elemental analysis of the films was performed by EDS using an Oxford Instruments X-MaxN 80 detector attached to a Zeiss Ultra Plus FE-SEM at an acceleration voltage of 15 kV.

4.2.5 UV-vis-NIR absorption spectroscopy. The optical absorption spectra of $Cs_2AgBi_2I_9$ thin films were measured using a Shimadzu UV-3600 spectrophotometer. The spectrum was recorded with a wavelength interval of 0.5 nm, and the monochromator slit width was set to 1 nm.

4.2.6 Transient absorption spectroscopy. Time-resolved transient absorption measurements were carried out on $Cs_2AgBi_2I_9$ thin films deposited on glass substrates using a pump–probe setup operated in transmission mode. Femtosecond laser pulses at 800 nm, with a pulse duration of 100 fs and a repetition rate of 1 kHz, were generated using a Libra F laser system (Coherent Inc.). The laser output was directed into a TOPAS-C optical parametric amplifier (Light Conversion Ltd) to generate excitation pulses at 400 nm. The excitation beam was modulated to 500 Hz using an optical chopper. The excitation power was adjusted to minimize photodegradation during data acquisition, typically within the range of approximately 100–500 μW. A white-light continuum probe was generated by focusing part of the laser beam into a water-filled cuvette. Transient absorption spectra were collected over the UV-visible region using an ExiPro spectrometer (CDP Inc.). The temporal window of the measurement was limited by the laser pulse width and delay-line range, allowing spectra to be recorded from approximately 0.2 ps to 6 ns. Global fits of kinetic traces were obtained using in-house multiexponential fitting software.

4.2.7 X-ray diffraction (XRD. X-ray diffraction (XRD patterns of the $Cs_2AgBi_2I_9$ films were collected using Cu K_α radiation on an Empyrean Alpha 1 high-resolution X-ray diffractometer, Malvern Panalytical.

4.3 Device fabrication and characterization

4.3.1 Photovoltaic device fabrication. Pre-patterned FTO-coated glass substrates, TEC15, 2.2 mm thick, OPV Tech.,

were employed as the front transparent electrodes. Prior to film deposition, the substrates were brushed with 2% mucasol solution and rinsed thoroughly with ultrapure water. They were subsequently cleaned by ultrasonication for 15 min each in ultrapure water, acetone, and 2-propanol. The cleaned substrates were dried under a stream of nitrogen. The compact TiO_2 electron-transport layer was prepared by spray pyrolysis at 450 °C. The spray solution was obtained by diluting 1.15 mL of titanium diisopropoxide bis(acetylacetonate), 75 wt% in 2-propanol, with 4.95 mL of 2-propanol. Deposition was carried out using 13 spray cycles, with a 20 s interval between each cycle. The substrates were then kept at 450 °C for 45 min to complete the formation of the compact TiO_2 layer. A mesoporous TiO_2 scaffold was deposited from a 150 mg mL^{-1} dispersion of 30 NR-D titania paste in ethanol. For each substrate, 80 μL of the dispersion was spin-coated at 4000 rpm for 30 s using an acceleration of 2000 rpm s^{-1}. The films were briefly heated at 100 °C and then calcined at 450 °C for 1 h with a 45 min temperature ramp. After calcination, the substrates were allowed to cool to 200 °C before being transferred into a nitrogen-filled glovebox for $Cs_2AgBi_2I_9$ deposition. The $Cs_2AgBi_2I_9$ absorber layer was formed by casting 60 μL of precursor solution onto each substrate and spin-coating at 4000 rpm for 20 s, with the acceleration completed within 5 s. After 6 s of spinning, 200 μL of chlorobenzene was introduced as an anti-solvent. The films were then annealed using a two-step thermal treatment: 130 °C for 5 min followed by 225 °C for 3 min. This annealing sequence was used to promote controlled solvent removal, nucleation, crystallization, and grain growth.

The effect of different HTMs on device performance was investigated using PPDT2FBT, PCPDTBT, doped Spiro-OMeTAD, and P3HT. PPDT2FBT and PCPDTBT were separately dissolved in 1,2-dichlorobenzene at a concentration of 10 mg mL^{-1} by stirring overnight at 60 °C. Each polymer solution, 70 μL, was dynamically spin-coated at 2500 rpm for 30 s, followed by thermal annealing at 80 °C for 10 min. Spiro-OMeTAD was dissolved in chlorobenzene at a concentration of 36.2 mg mL^{-1} and doped with 4-*tert*-butylpyridine (*t*BP), Li-TFSI solution (520 mg mL^{-1} in acetonitrile), and FK209 Co(III) solution (300 mg mL^{-1} in acetonitrile). For 1000 μL of Spiro-OMeTAD solution, 14.4 μL of *t*BP, 8.8 μL of Li-TFSI solution, and 14.5 μL of FK209 Co(III) solution were added. The doped Spiro-OMeTAD layer was deposited by dynamically spin-coating 80 μL of solution at 1800 rpm for 30 s. For P3HT-based devices, P3HT was dissolved in chlorobenzene at a concentration of 10 mg mL^{-1} by stirring for 2 h at 80 °C. The P3HT solution, 80 μL, was dynamically spin-coated at 2500 rpm for 30 s and then annealed at 80 °C for 10 min. Finally, the devices were completed by thermally evaporating 100 nm Au electrodes under a vacuum of 6×10^{-6} mbar.

4.3.2 Photovoltaic device characterization. The photovoltaic performance of the fabricated devices was evaluated under simulated AM 1.5G illumination using an A+ A+ A+ SINUS-70 LED solar simulator from Wavelabs. Current density–voltage (*J–V*) characteristics and stabilized power output measurements were recorded under ambient conditions using a Litos Lite parallel *J–V* system from Fluxim. Stabilized power output was obtained by maximum power point tracking. *J–V* scans were recorded at a scan rate of 50 mV s^{-1}, and the device active area was defined using 10 mm^2 aperture masks.

Indoor photovoltaic measurements were performed under controlled illumination using an adjustable Philips HUE white LED bulb operated through the Philips Hue Essential App. The devices were placed inside a black box under ambient conditions to minimize stray-light reflections. Before each measurement, the WLED source was allowed to stabilize, and the spectral irradiance, illuminance, incident power density, and correlated colour temperature (CCT) were measured at the device plane using a BTS256-WF spectroradiometer from Gigahertz-Optik. The incident power density was obtained by integrating the measured spectral irradiance over the relevant wavelength range. Indoor *J–V* characteristics were recorded using a Keithley 2450 source-measure unit in a four-wire configuration at a scan rate of 50 mV s^{-1}. The active area was defined using the same 10 mm^2, 400 μm-thick aperture mask for all controlled indoor measurements to minimize photocurrent overestimation arising from edge effects, scattered light, or illumination of inactive regions.

Indoor measurements were carried out under 6500 K, 1000 lux WLED illumination for the main device comparison, with additional measurements at other WLED colour temperatures where specified. For maximum-power-point measurements under indoor illumination, the device was held at the maximum-power voltage, and the stabilized power output was recorded under continuous WLED illumination. The reported stabilized indoor PCE values were calculated using the measured incident power density at the device plane.

Mixed office-light measurements were performed as a proof-of-concept assessment of device operation under practical indoor illumination. A representative $Cs_2AgBi_2I_9$/PPDT2FBT device was measured in an office environment under ambient mixed lighting composed of room WLED illumination, local workspace lighting, and diffuse daylight. For each office-light measurement, the device-plane spectral irradiance, illuminance, incident power density, and CCT were recorded simultaneously with the photovoltaic measurement using the BTS256-WF spectroradiometer. The same 10 mm^2 aperture mask used for the controlled indoor measurements was used during the office-light *J–V* measurements, which were recorded at a scan rate of 50 mV s^{-1}.

External quantum efficiency measurements were performed in the dark using a QuantX-300 system from Newport. The integrated short-circuit current density values were calculated by integrating the measured EQE spectra with the incident photon flux of either the AM 1.5G spectrum or the corresponding indoor light spectra recorded using the BTS256-WF spectroradiometer.

4.3.3 Transient photovoltage and electrochemical impedance spectroscopy measurements. EIS measurements were performed using an Ivuum Electrochemical Workstation at 0 V applied bias in room light. In EIS, an AC amplitude of 20 mV was applied, and the frequency range was varied from 0.5 MHz to 5 Hz to measure the impedance of the devices. The EIS data were fitted with Zview software. To assess the recombination

time constant of the devices, we conducted TPV measurements using a homemade setup with a white light source at an intensity of 1-Sun. The transient photovoltage decays were fitted with a mono-exponential decay function.

4.3.4 Transient photocurrent measurements. Transient photocurrent (TPC) measurements were performed using the PAIOS characterization system (Fluxim AG). The devices were measured under short-circuit conditions using a white light pulse with a duration of 1.5 μs as the excitation source. The decay of the transient photocurrent generated after the light pulse was monitored to investigate the charge extraction and carrier transport dynamics of the devices.

5 Computational details

We carried out density functional theory calculations with periodic boundary conditions (PBC) employing the light-tier1 basis set of numerical atom-centered orbitals (NAO)[42] for each atom for geometry optimization and the electrons are described by the zero-order regular approximation (atomic ZORA)[43] as implemented in the Fritz Haber Institute *ab initio* molecular simulations (FHI-aims) code.[44] A self-consistency threshold of 1×10^{-6} eV is set for the total energy. We use the Perdew–Burke–Erzenhof (PBE) exchange correlation functional[45,46] for all geometry optimizations, including the Tkatchenko–Scheffler (TS) correction[47] to take into account the van der Waals dispersion forces. Our fully relaxed structures present maximum forces acting on each atom below 0.02 eV $Å^{-1}$. To investigate the electronic properties, we employ the HSE06 level of theory, because it is fundamental to reproduce the experimental gap values. We use a $3 \times 3 \times 1$ *k*-point sampling for the slab models.

We compute the donor–acceptor couplings at HSE06 level of theory, as implemented in CP2K.[48] Charge transfer calculations were performed considering all the atoms of the interfaces. Double-ζ basis sets with one set of polarization functions (double-ζ valence polarized, DZVP) were employed, along with a plane wave cutoff of 300 Ry. The Goedecker–Teter–Hutter (GTH) pseudopotentials were used to represent the core electrons.

Author contributions

M. K. and A. A. conducted experiments on the film processing of bismuth-based perovskite-inspired materials. M. K. performed the structural analyses, including X-ray diffraction (XRD), scanning electron microscopy (SEM), and energy-dispersive X-ray spectroscopy (EDS). M. K. carried out device fabrication and characterization under various illumination conditions. In addition, M. K. conducted FE-SEM and EDS analyses of the thin films. M. K. wrote the first draft of the manuscript together with G. K. G. A. P., A. B. M. G., and M. P. performed and analysed the density functional theory (DFT) calculations for the interface study. J. K. performed and analysed the transient absorption, UV-vis, and atomic force microscopy (AFM) measurements. R. Kumar and H. C. conducted the electrochemical impedance spectroscopy (EIS) and transient photovoltage (TPV) measurements. A. A. performed the transient photocurrent (TPC) measurements and assisted with device fabrication and characterization. B. D. carried out the Raman spectroscopy measurements. M. K., G. K. G., and P. V. conceptualised the indoor photovoltaics study and developed the indoor characterization methodology. P. V. managed and supervised the overall work. All authors edited the review together.

Conflicts of interest

There are no conflicts to declare.

Data availability

The experimental and computational data supporting the findings of this work are available in the main article and its supplementary information (SI). The SI includes additional figures and tables on thin-film characterization, device architecture, photovoltaic performance, indoor WLED measurements, statistical device parameters, stabilized power output, DFT-based interface analysis, density of states, energy-level calculations, differential resistance, transient photovoltage, and photovoltaic, computational, recombination, EIS, and diode parameters. Supplementary information is available. See DOI: https://doi.org/10.1039/d6ta04885d.

Acknowledgements

M. K. acknowledges funding from SPINIP, HORIZON-MSCA-2023-PF-1 (Grant No. 101150357). Joshua K. G. Karlsson acknowledges Tampere University and the Tampere Institute for Advanced Study for research funding. P. V. acknowledges the Research Council of Finland (Decision No. 347772). This work is part of the Research Council of Finland Flagship Programme, Photonics Research and Innovation (PREIN) (Decision No. 346511). G. K. G., A. A., and P. V. gratefully acknowledge support from the SPOT-IT project funded under the CET Partnership through the Clean Energy Transition Partnership Joint Call 2022 for research proposals, co-funded by the European Commission (Grant Agreement No. 101069750) and the funding organizations listed by the CET Partnership. This project was supported by funding from the European Union's Horizon Europe research and innovation programme through the Marie Skłodowska-Curie Grant Agreement No. 101169056. This work made use of Tampere Microscopy Center facilities at Tampere University.

References

1 G. K. Grandhi, G. Koutsourakis, J. C. Blakesley, F. De Rossi, F. Brunetti, S. Öz, A. Sinicropi, M. L. Parisi, T. M. Brown, M. J. Carnie, R. L. Z. Hoye and P. Vivo, *Nat. Rev. Clean Technol.*, 2025, **1**, 132–147.

2 J. Xu, A. Chakraborty, Z. Skafi, V. Singh, D. Thakur, E. Joseph, S. Hou, Z. Xu, X. Liu, X. Xu, M. Ouyang and T. M. Brown, *EES Sol.*, 2026, **2**(3), 537–587.

3 Y. Li, J. Wang, Z. Jiang, Y. Sun, D. Wu, A. Bahtiar, Y. Yang and D. Zhao, *Mater. Today*, 2025, **90**, 495–518.
4 R. L. Z. Hoye, G. Koutsourakis, M. Freitag, Z. Jehl Li-Kao, T. Österberg, S. Aliwell, M. Bellanger, T. M. Brown, F. Brunetti, M. J. Carnie, A. Chakraborty, G. Grancini, P. Kärhä, M. Kauer, T. Kirchartz, C.-T. Lin, M. Lira-Cantú, Y.-S. Long, S. Öz, S. R. Raga, E. Saucedo, P. Vivo, S. W. Leow, K. Wojciechowski, A. Zampetti, R. Zhou, S. Züfle and G. Burwell, *Joule*, 2025, **9**, 102127.
5 G. K. Grandhi, B. Damien, Z. Skafi, K. Sasitharan, H. Kanaan, H. Alkhatib, S. B. Dkhil, M. J. Carnie, M. Freitag, T. M. Brown and P. Vivo, *ACS Energy Lett.*, 2026, **11**, 2474–2490.
6 R. Datt, P. Caprioglio, S. Choudhary, W. Lan, H. Snaith and W. C. Tsoi, *JPhys Energy*, 2024, **6**, 025014.
7 J. M. Jailani, A. Luu, E. Salvosa, C. Clegg, V. P. Kamalon, B. Nasrollahi, I. Valitova, S. B. Meier, A. M. Shore, B. H. Hamadani and V. Pecunia, *Joule*, 2025, **9**, 102126.
8 I. M. Asuo, A. Mahdavi Varposhti, C. C. F. Kumachang, G. K. Grandhi, V. Pecunia, T. M. Brown, P. Vivo and N. Y. Doumon, *Adv. Energy Mater.*, 2026, **16**, e06091.
9 G. K. Grandhi, N. S. Manikanta Viswanath, M. Righetto, S. Domenici, M. Krishnaiah, M. Moroni, A. Pecoraro, A. B. Muñoz-García, M. Pavone, L. Malavasi, T. Gatti and P. Vivo, *J. Mater. Chem. A*, 2026, **14**, 60–89.
10 N. Lamminen, J. Lahtinen, M. Krishnaiah, J. Karlsson, M. Saju, G. K. Grandhi and P. Vivo, *ACS Energy Lett.*, 2025, **10**, 3415–3418.
11 V. Holappa, G. K. Grandhi, N. Lamminen, R. Suhonen, T. M. Kraft and P. Vivo, *npj Flexible Electron.*, 2025, **10**, 6.
12 J. Lee, J. Park, B.-C. Jeon, S. Lim, J.-Y. Back, J. Kim and T. Moon, *ACS Sustainable Chem. Eng.*, 2024, **12**, 14396–14401.
13 M. Krishnaiah, K. Singh, S. Monga, A. Tripathi, S. Karmakar, R. Kumar, C. Tyrpenou, G. Volonakis, D. Manna, P. Mäkinen, K. V. Adarsh, S. Bhattacharya, G. K. Grandhi, K. D. M. Rao and P. Vivo, *Adv. Energy Mater.*, 2025, **15**, 2404547.
14 M. Hossain, K. Singh, A. Narwal, M. S. Sheikh, S. K. Reddy, K. Vankayala, A. Singh, S. Khan, S. Khan, P. K. Velpula, M. Chirumamilla, S. S. R. K. C. Yamijala, G. K. Grandhi, P. Vivo and K. D. M. Rao, *Chem. Mater.*, 2024, 4c01045.
15 G. K. Grandhi, S. Toikkonen, B. Al-Anesi, V. Pecunia and P. Vivo, *Sustainable Energy Fuels*, 2023, **7**, 66–73.
16 G. K. Grandhi, D. Hardy, M. Krishnaiah, B. Vargas, B. Al-Anesi, M. P. Suryawanshi, D. Solis-Ibarra, F. Gao, R. L. Z. Hoye and P. Vivo, *Adv. Funct. Mater.*, 2024, **34**, 2307441.
17 S. Wang, B.-C. Kang, S.-J. Park, T.-J. Ha and L. Krishnan Jagadamma, *JPhys Mater.*, 2023, **6**, 024004.
18 E. Serpetzoglou, I. Konidakis, G. Kourmoulakis, I. Demeridou, K. Chatzimanolis, C. Zervos, G. Kioseoglou, E. Kymakis and E. Stratakis, *Opto-Electron. Sci.*, 2022, **1**, 210005.
19 E. Serpetzoglou, I. Konidakis, T. Maksudov, A. Panagiotopoulos, E. Kymakis and E. Stratakis, *J. Mater. Chem. C*, 2019, **7**, 12170–12179.
20 C.-F. Li, S.-H. Cheng, H.-C. Cha, S.-Y. Chung, D. Glowienka, C.-M. Chuang and Y.-C. Huang, *ACS Appl. Energy Mater.*, 2024, **7**, 10203–10211.
21 T. L. Nguyen, H. Choi, S.-J. Ko, M. A. Uddin, B. Walker, S. Yum, J.-E. Jeong, M. H. Yun, T. J. Shin, S. Hwang, J. Y. Kim and H. Y. Woo, *Energy Environ. Sci.*, 2014, **7**, 3040–3051.
22 J. Jiménez-López, W. Cambarau, L. Cabau and E. Palomares, *Sci. Rep.*, 2017, **7**, 6101.
23 B. Xiao, P. Calado, R. C. I. MacKenzie, T. Kirchartz, J. Yan and J. Nelson, *Phys. Rev. Appl.*, 2020, **14**, 024034.
24 A. Pecoraro, F. Fasulo, M. Pavone and A. B. Muñoz-García, *Chem. Commun.*, 2023, **59**, 5055–5058.
25 J. Haruyama, K. Sodeyama, I. Hamada, L. Han and Y. Tateyama, *J. Phys. Chem. Lett.*, 2017, **8**, 5840–5847.
26 A. Pecoraro, F. Fasulo, M. Pavone, A. Di Carlo and A. B. Muñoz-García, *J. Mater. Chem. A*, 2026, **14**, 313–319.
27 D. Bi, L. Yang, G. Boschloo, A. Hagfeldt and E. M. J. Johansson, *J. Phys. Chem. Lett.*, 2013, **4**, 1532–1536.
28 Z. Jiang, T. Du, C. Lin, T. J. Macdonald, J. Chen, Y. Chin, W. Xu, B. Ding, J. Kim, J. R. Durrant, M. Heeney and M. A. McLachlan, *Adv. Mater. Interfaces*, 2023, **10**, 2201737.
29 S. Zhu and Y. Li, *Solid-State Electron.*, 2020, **173**, 107903.
30 A. These, L. J. A. Koster, C. J. Brabec and V. M. Le Corre, *Adv. Energy Mater.*, 2024, **14**, 2400055.
31 Y. Peng, T. N. Huq, J. Mei, L. Portilla, R. A. Jagt, L. G. Occhipinti, J. L. MacManus-Driscoll, R. L. Z. Hoye and V. Pecunia, *Adv. Energy Mater.*, 2021, **11**, 2002761.
32 G. G. Jeon, D. S. Lee, M. J. Choi, Y. Seo, S. Huang, J. H. Kim, S. S. Shin and J. Kim, *EcoMat*, 2024, **6**, e12455.
33 L. K. Jagadamma and S. Wang, *Front. Chem.*, 2021, **9**, 632021.
34 Q. Ma, Y. Wang, L. Liu, P. Yang, W. He, X. Zhang, J. Zheng, M. Ma, M. Wan, Y. Yang, C. Zhang, T. Mahmoudi, S. Wu, C. Liu, Y.-B. Hahn and Y. Mai, *Energy Environ. Sci.*, 2024, **17**, 1637–1644.
35 O. J. Sandberg, K. Tvingstedt, P. Meredith and A. Armin, *J. Phys. Chem. C*, 2019, **123**, 14261–14271.
36 D. Kiermasch, A. Baumann, M. Fischer, V. Dyakonov and K. Tvingstedt, *Energy Environ. Sci.*, 2018, **11**, 629–640.
37 Z. S. Wang, F. Ebadi, B. Carlsen, W. C. H. Choy and W. Tress, *Small Methods*, 2020, **4**, 2000290.
38 G. R. Neupane, J. F. Roller, S. M. Thon, S. Fu, Z. Song, Y. Yan and B. H. Hamadani, *J. Phys. Chem. C*, 2024, **128**, 16372–16379.
39 Z.-E. Shi, T.-H. Cheng, C.-Y. Lung, C.-W. Lin, C.-L. Wang, B.-H. Jiang, Y.-S. Hsiao and C.-P. Chen, *Chem. Eng. J.*, 2024, **498**, 155512.
40 A. Dabuliene, Z.-E. Shi, K. Leitonas, C.-Y. Lung, D. Volyniuk, K. Kaur, V. Matulis, D. Lyakhov, D. Michels, C.-P. Chen and J. V. Grazulevicius, *ACS Appl. Mater. Interfaces*, 2024, **16**, 30239–30254.
41 D. Nečas and P. Klapetek, *Open Phys.*, 2012, **10**, 181–188.
42 V. Havu, V. Blum, P. Havu and M. Scheffler, *J. Comput. Phys.*, 2009, **228**, 8367–8379.
43 E. Van Lenthe, A. Van Der Avoird and P. E. S. Wormer, *J. Chem. Phys.*, 1998, **108**, 4783–4796.

44 V. Blum, R. Gehrke, F. Hanke, P. Havu, V. Havu, X. Ren, K. Reuter and M. Scheffler, *Comput. Phys. Commun.*, 2009, **180**, 2175–2196.
45 J. P. Perdew, K. Burke and Y. Wang, *Phys. Rev. B: Condens. Matter Mater. Phys.*, 1996, **54**, 16533–16539.
46 J. P. Perdew, K. Burke and Y. Wang, *Phys. Rev. B: Condens. Matter Mater. Phys.*, 1998, **57**, 14999.
47 A. Tkatchenko and M. Scheffler, *Phys. Rev. Lett.*, 2009, **102**, 073005.
48 Z. Futera and J. Blumberger, *J. Phys. Chem. C*, 2017, **121**, 19677–19689.

